

Self-organization of cavity solitons in Brillouin–Kerr ring resonators

Corentin Simon,¹ Matteo Conforti,² Loïc Van Bellinghen,¹ Maxime Fournier,¹ Arnaud Mussot,² François Leo,¹ and Simon-Pierre Gorza¹

¹*OPERA-photonics, Université libre de Bruxelles (U.L.B.),*

50 Avenue F. D. Roosevelt, CP 194/5, B-1050 Brussels, Belgium

²*University of Lille, CNRS, UMR 8523-PhLAM Physique des Lasers, Atomes et Molécules, F-59000, Lille, France*

(Dated: 5. March 2026)

We report on the interaction between stimulated Brillouin scattering and temporal cavity solitons (CSs) in doubly resonant ring resonators. Our experiments are performed in coherently driven passive optical-fibre resonators. We demonstrate that the interplay between four-wave mixing and cascade Brillouin lasing spontaneously generates patterns of CSs on a temporal grid at twice the Brillouin-shift. These patterns are shown to be highly stable owing to a long-range locking mechanism mediated by the acoustic oscillation generated by the solitons. We introduce a unified mean-field model of the cavity to describe the dynamics between the coupled forward and backward waves under coherent driving. This model reproduces very well the experiments and explains the paracrystalline structures of the soliton pattern. Our findings significantly advance the understanding of hybrid Brillouin-Kerr optical frequency combs.

Introduction—Temporal dissipative solitons are particle-like excitations propagating endlessly in optical nonlinear resonators [1–5].

Among them, temporal cavity solitons (CS) emerge in coherently driven Kerr resonators, naturally enforcing phase locking between the pulses and the external driving field.

Over the past two decades, they have attracted considerable attention due to their broad impact across photonics and precision-measurement technologies [6–10].

In addition to the Kerr-induced parametric interaction that underpins CSs generation, stimulated Brillouin scattering (SBS) is another prominent nonlinear effect that manifests in optical waveguides [11, 12]. SBS, which couples optical fields to an acoustic wave, provides a narrow-band optical gain that enables ultra-coherent lasing [13–17], thereby supporting a wide range of applications [18–23].

Brillouin scattering has recently attracted renewed attention due to the rich nonlinear dynamics that stem from the interplay between Brillouin lasing and four-wave mixing, particularly in the context of optical frequency-comb generation. Non-reciprocal fiber ring resonators have been explored under both single [24] and multi-wavelength excitation [25–27], revealing soliton formation with anomalous dispersion [28]. Brillouin–Kerr frequency combs have also been realized in high-Q fiber Fabry–Pérot cavities [29–32]. Internally pumped counter-propagating cavity solitons enabled by Brillouin lasing in microdisks have demonstrated thermal self-stabilization of the pump and low-noise operation [33], as well as deterministic single-soliton states generation [34]. Besides, multi-soliton Kerr combs propagating in opposite directions under a single external pump have been reported in silica microspheres [35].

Investigations of the interaction between cavity solitons and Brillouin scattering have thus far been lim-

ited either to non-reciprocal cavities, i.e., to non-resonant pumping, or to short resonators whose free-spectral range exceeds the Brillouin-gain bandwidth. Earlier works on CW-pumped fiber cavities indeed suppressed Brillouin lasing via optical isolation [3, 36], despite the CS pump power threshold can be reached first in low-loss resonators. Yet, owing to their robust localized nature, the collective dynamics of multiple cavity solitons are expected to be particularly susceptible to Brillouin scattering. The formation of multi-soliton bound-state patterns is a universal mechanism observed in coherently driven Kerr cavities [36–39], as well as in other dissipative systems such as mode-locked lasers [40, 41]. Hence, the longitudinal acoustic wave emitted by solitons could provide an efficient long-range binding mechanism, a possibility yet to be explored.

In this Letter, we investigate cavity-soliton dynamics in doubly resonant Brillouin laser cavities. We introduce a new set of equations that capture the Brillouin–Kerr interaction in driven ring resonators, simplifying previous models [42, 43]. We compare the model’s predictions with experiments in long-fiber resonators and use them to elucidate the spontaneously emerging robust soliton patterns and the associated Kerr comb.

Results—

Our theoretical analysis of the intracavity nonlinear dynamics, together with numerical simulations, relies on the coupled mean-field equations A1-A2 provided in the End Matter, which are established for doubly resonant Brillouin–Kerr ring lasers. These equations describe the round-trip evolution of the slowly varying envelopes of the driven forward (ψ_F) and backward (ψ_B) fields.

To get insight into the interplay between CSs and Brillouin lasing, let us analyze the interaction between a single coherently driven forward CS and the first-order Stokes wave S_1 [i.e. $\psi_B = S_1 \exp(i\Omega_b \beta_1 z)$, with $\Omega_b = 2\pi\nu_b$, the Brillouin shift frequency, β_1 , the inverse

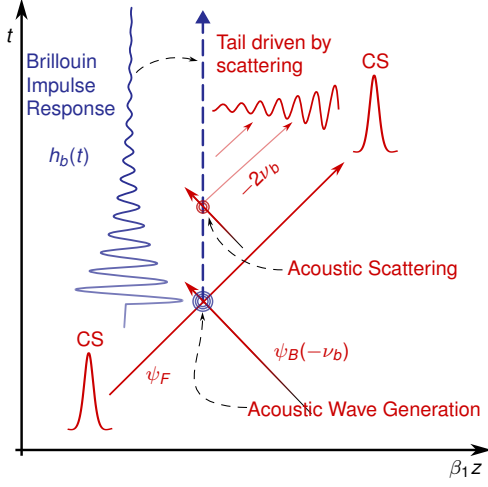


Figure 1. Space–time schematic representation of the trailing tail formation behind a CS. The CS locally excites an acoustic wave with the Brillouin impulse response $h_b(t)$, upon which S_1 is scattered, resulting in the generation of a decaying trailing wave pinned to the soliton.

of the group velocity and z , the position].

We first note that the soliton spectrum (\sim THz) is much wider than the Brillouin gain bandwidth (\sim 50 MHz). When the resonator free spectral range is smaller than the Brillouin bandwidth, the contribution of the CS to the Brillouin interaction term in the equation of ψ_F is proportional to $h_b(z_{CS} - z) \exp[i\Omega_b\beta_1(z_{CS} - z) + i\phi_{CS}]$ (as detailed in the End Matter). Here, h_b denotes the spatial Brillouin response, and z_{CS} , ϕ_{CS} are the soliton position and phase, respectively.

This term acts as an additional coherent drive, composed of two spectral components: one at the frequency of the external driving field and one shifted by $-2\nu_B$. The resulting trailing signal, by beating with the forward background field at the driving frequency (S_0), generates a stationary pattern in the CS reference frame (see schematic representation in Fig.1). This mechanism creates a long-range oscillating interaction potential with a characteristic timescale of about 100 ns [37], enabling mutual interactions among thousands of solitons and potentially facilitating the formation of soliton crystals within the resonator.

The experiments are performed in a 30.7-m-long fiber ring resonator (3.5% loss, 2.55×10^9 Q-factor) operating in the anomalous-dispersion regime and driven by a highly coherent continuous-wave (CW) laser through a 1% input coupler (see more details in the End Matter). We start by studying the spontaneous formation of CSs in the presence of cascade Brillouin lasing. When the intracavity power increases, it eventually crosses the

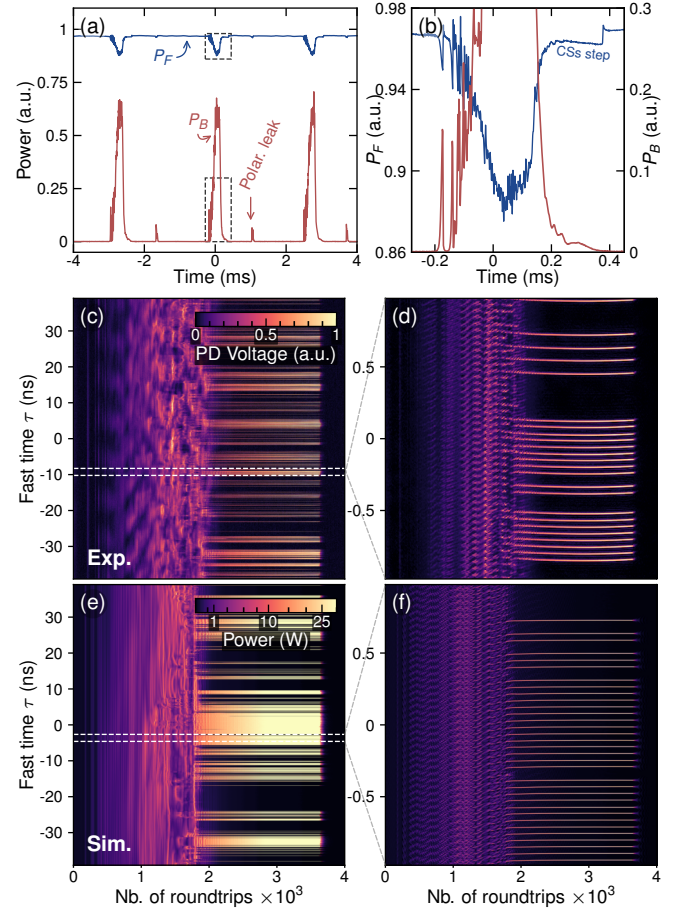


Figure 2. (a) Transmitted (P_F) and backward (P_B) signals when scanning the frequency of a laser over multiple resonances (forward detuning scan rate 2.3 rad/ms). The transmission shows the expected tilted nonlinear resonance, followed by a single soliton step. (b) Close-up view of a single resonance. This step co-exists with a weak backward Brillouin lasing signal. (c) Dynamics of the output forward signal, recorded with a high-bandwidth oscilloscope after filtering the CW driving component. The formation dynamics of individual solitons are visible in the zoomed-in view (d). (e,f) The simulation with our mean-field model [Eqs.A1-A2] reproduces very well the whole dynamics (2.3 rad/ms). Raman interaction, which slightly bends CS's trajectory in panel (d), is not included in the simulation for simplicity.

Brillouin laser threshold. Beyond, the first-order backward Stokes wave S_1 is generated. With a further increase in driving power P_{in} , or with deeper tuning into resonance, the system crosses successive thresholds that generate odd backward and even forward Stokes orders S_j . This cascade could hinder the spontaneous emergence of CSs during a detuning scan. Indeed, the mean-field model without Brillouin shows that a parametric

Kerr gain $P_{\text{cav}}\gamma L > \Lambda/2$ is required for spontaneous CSs formation. Although the Brillouin cascade has little impact on the average loss experienced by CSs, it prevents the build-up of the CW average power P_{cav} . Consequently, we only detect CSs spontaneous generation above $P_{\text{in}} \gtrsim 500$ mW while a threshold of 16 mW is predicted without Brillouin lasing. The nonlinear resonances of the forward and backward waves are shown in Fig. 2(a-b) for a driving power of 600 mW. We observe a shallow resonance in the average power of the forward signal measured in the through port, despite the resonator being close to critical coupling. Simultaneously, backward lasing occurs, in agreement with the previous analysis of the Brillouin cascade. At higher detunings, i.e., beyond the strong backward lasing peak, the forward output power exhibits the characteristic signature of CS formation, known as the soliton step. Resonance-scan measurements uncover complex soliton formation dynamics [see Figs. 2(c-d)], with nanosecond-scale transient structures that determine the final CS density as the cascade dissipates. For convenience, we introduce the fast-time $\tau = -\beta_1 z$, which refers to the time over a single cavity round-trip. Zooming in, we see the spontaneous emergence of patterns with occasional stochastic defects. Strikingly, it consists of individual solitons on a lattice of period $1/2\nu_b$. This period corresponds to the fundamental beating period between even Stokes waves ($2\nu_b = 21.7$ GHz) and arises from the dynamics of the Brillouin cascade as the resonance is scanned (see Supplemental Material Fig.S3(c)). Numerical simulations reproduce the resulting soliton patterns with very good agreement [see Figs. 2(e,f) and Supplemental Material Fig.S3(a-b)], which validate our mean-field model Eqs. A1-A2.

The long-term stability of the soliton pattern is then studied. Oscilloscope traces, at a detuning $\delta \approx 0.5$, reveal the high stability of the pattern over minutes (Fig.3a), only limited by the locking range. The backward-recorded spectrum indicates that S_1 circulates within the cavity under this stable regime (Fig.3c). Yet, at higher detunings, it vanishes, and we observe a rapid breaking of the periodicity and the well-known bunching dynamics of CSs stemming from transverse acoustic waves [44] (not shown). This highlights the importance of Brillouin-mediated long-range mutual interactions in maintaining solitons on a regular grid.

Perfect cavity-soliton crystallization generates sharp optical spectral lines through multi-soliton coherent interference [38]. Stochastic vacancies in such soliton crystals manifest themselves as reduced overall visibility in the optical spectrum. Figure 3b shows the spectrum, measured at the cavity output, after filtering the pump-laser frequency. In addition to the intense S_2 line, it features narrow peaks separated by a wavelength shift corresponding to $2\nu_b$, in agreement with the temporal pattern. Their visibility, however, decreases away from the pump,

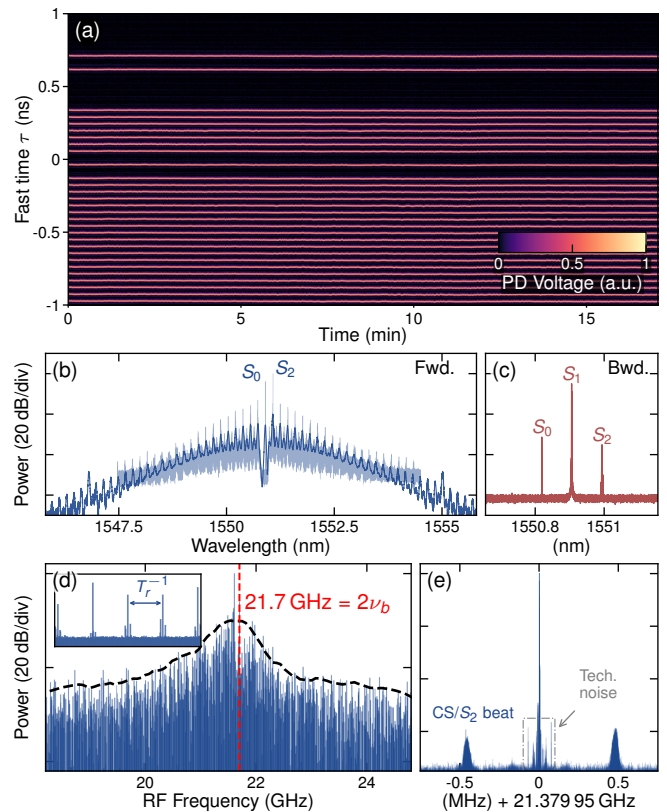


Figure 3. (a) Oscilloscope measurements at the cavity output showing the long-term stability of the soliton pattern ($\delta \approx 0.49$). (b) Optical spectrum measured in the through port of the cavity coupler, after pump filtering. Light blue, high resolution (RBW = 0.16 pm) and, dark blue, low resolution (RBW = 30 pm). (c) Same for the backward signal at high resolution. (d) Radiofrequency spectrum corresponding to (b) (different realization). Inset: fine teeth structure of the wide comb. (e) Zoom around one RF tooth.

suggesting irregular soliton spacing. This is confirmed in the electrical spectrum of the pulse train (Fig. 3d). It consists of thousands of beat notes spaced at multiples of the cavity FSR, with a relatively flat structure due to vacancies. It also shows a broad peak at $2\nu_b$, thus lacking the sharp RF beat note expected for a perfect crystal containing only vacancies. Additionally, a closer inspection reveals broadened sidebands at ± 470 kHz from the main RF peaks (see e.g. Fig.3e).

They originate from the frequency shift between S_2 and the closest soliton comb frequency. S_2 , which lies on a cavity mode, indeed does not coincide with a tooth of the soliton comb because of the pump detuning. As a result, the background, modulated by the interference between S_0 and S_2 , drifts in the soliton reference frame. This causes the CSs to oscillate in amplitude at the frequency $\delta/(2\pi T_R)$, with T_R the round-trip time. The

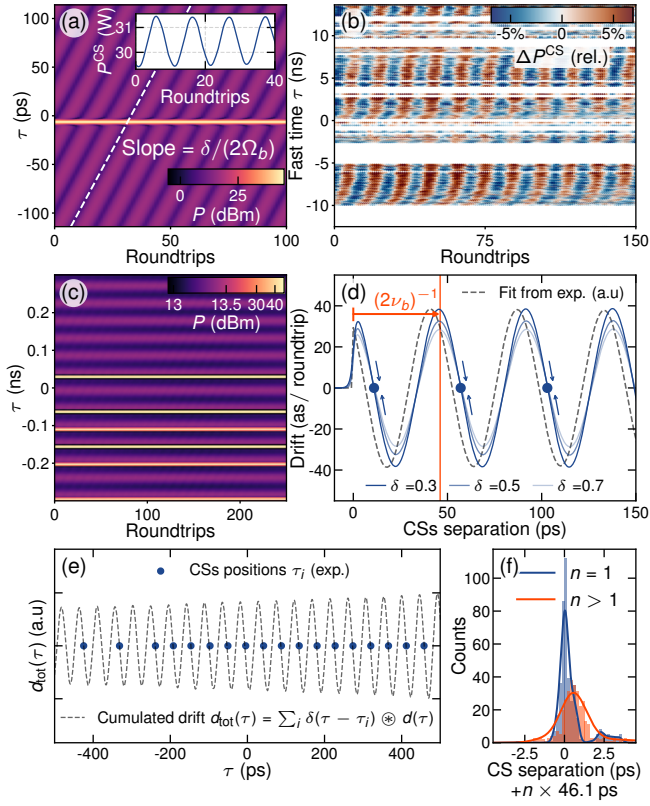


Figure 4. (a) Simulation of a CS showing its oscillation induced by the drifting modulated background from the $S_0 - S_2$ beating. Inset: soliton peak power variation. (b) Experimental measurement of the oscillation of the CSs. Each point of the scatter plot corresponds to a single CS. (c) Simulated intracavity power for spontaneously generated CSs, after numerical filtering of S_2 . The weak modulation at $2\nu_b$, stationary in the CSs reference frame and responsible for their locking, can be seen. (d) Theoretical soliton drift induced by the interaction between a CS located at $\tau = 0$ and S_1 , computed from Eqs. A1-A2 (solid lines). Stable equilibrium points are indicated. The dashed line shows our simplified analytical model of the drift, fitted to the experimental CS positions. (e) Reconstructed cumulated drift from the fitted model and experimental CSs positions computed from the oscilloscope trace recorded over a round-trip once the pattern is stabilized. (f) Distribution of the experimental delay between two consecutive solitons, separated by a single ($n = 1$) or multiple ($n > 1$) lattice period $1/2\nu_b = 46.1$ ps.

beating frequency measured in the RF spectrum gives a detuning $\delta = 0.44(1)$, in agreement with the detuning estimated from the fit of the optical spectrum [$\delta = 0.45(2)$]. Interestingly, the beating peak width provides a measurement of the detuning stability. We extract a detuning standard deviation of ~ 10 mrad for our dedicated stabilization scheme (see Supplemental Material).

We exploit the time-domain oscillations to probe the local distance between solitons over the entire cavity round-trip, and gain insight into their locking mechanism. The numerical simulation reported in Fig. 4a displays the drifting modulated background, along with a single oscillating soliton. For regularly spaced CSs, the phase of the oscillations would be constant or linearly varying with position across the pulse sequence. This is not observed in the experiment. Instead, the direct measurement of the oscillations (Fig. 4b) shows that closely spaced CSs are not perfectly equidistant, although their oscillation phases exhibit a certain degree of correlation. In contrast, more distant solitons appear to be randomly positioned. This confirms the irregular spacings in the self-organization of the solitons, already seen in the optical and RF spectra. Filtering out, in simulations, the background modulation arising from the $S_0 - S_2$ beating reveals a residual stationary pattern (Fig. 4c). This pattern originates from the Brillouin coupling between S_1 and each soliton, as predicted, which drives the oscillating tails responsible for its formation. The comparison between the CSs position and the modulation indicates that this pattern underlies the CS pinning mechanism, in agreement with the observation that the presence of S_1 is required for long-term stabilization. The locking is similar to the well-established mechanism attracting CSs to extrema of an external drive amplitude or phase modulation [45], and provides a many-body interaction between CSs. The theoretical drift that a single soliton induces on another can be determined by projecting the corresponding drive term onto the CS neutral mode [46]. This analysis reveals a one-sided CS-to-CS interaction, leading to stable points arranged in a lattice with a period of $1/2\nu_b$ (Fig. 4d). For comparison purposes, we fit a similar interaction function [$d(\tau) = \sin(a\tau + b) \exp(-c\tau)u(\tau)$, with fit parameters a, b, c and with $u(\tau)$ the Heaviside function] to the experimental CSs position distribution over the roundtrip (Fig. 4e). The period (a) of the optimal fit and decay (c) parameters matches very well the computed one (Fig. 4d), with only a small discrepancy for the shift (b), which we believe stems from the coupling between the Raman self-frequency shift, not accounted for in the theoretical analysis, and the CSs oscillations. Nonetheless, this confirms that the separation between the leading soliton and the first stable point is shorter than a lattice unit of length $1/2\nu_b$. This shift results in distortions of the equilibrium position from a perfect lattice behind each vacancy owing to the cumulative effect of many CSs. Consequently, in the experiments, CSs sit on a disordered one-dimensional lattice, with a paracrystalline-like structure in time governed by the number and position of vacancies (Fig. 4f) [47] (see also Supplemental Material), while CSs localization on a perfect crystal lattice would occur in vacancy-less patterns.

Conclusion—We investigated the interplay between Brillouin lasing and Kerr-comb formation in coherently

driven, doubly resonant ring cavities. We introduced a unified mean-field model for the forward and backward waves that explicitly accounts for their nonlinear coupling through Brillouin scattering. This coupling is shown to induce an effective many-body interaction mechanism. We experimentally demonstrated that it stabilizes individual CSs on a temporal lattice of period $\approx 1/2\nu_b$, resulting in long-lived, robust arrangements that would not otherwise exist. We stress that this effect differs from the well-known acoustically induced interaction responsible for pulse bunching in mode-locked lasers [48] and driven fiber Kerr-cavities [36], which we also observed in our experiments, though only below the first Brillouin threshold. However, the shape of the interaction potential from a single soliton, together with the presence of vacancies, gives rise to a paracrystalline time structure. It is characterized by small stochastic cumulative distortions from perfect lattice ordering, which results in a broadened RF beatnote at $2\nu_b$.

Vacancy-free CS patterns would result in distortion-free periodic soliton crystals with low frequency jitter, arising from the mutual coupling of thousands of CSs, since the fundamental jitter scales as $1/\sqrt{N}$ for N coupled pulses (by comparison, CSs coupled through soliton-radiated waves, such as Kelly sidebands, would involve only a few tens of pulses.) This property makes such states attractive for applications in low-noise optical frequency combs and low-noise radio-frequency generation. Unlike other schemes, the reduced linewidth of the Brillouin laser is not directly exploited here [33], as the solitons are driven by the pump laser. However, the S_2 Stokes wave induces CS oscillations at a frequency linked to the detuning, opening a route toward further stabilization of the driving laser via the resulting heterogeneous RF beat signal. Finally, our mean-field model closely matches the experimental observations and provide a unified theoretical framework to further study single and multiple Kerr combs in fiber and integrated ring resonators [33–35].

ACKNOWLEDGMENT

We acknowledge funding by the Fonds National de la Recherche Scientifique – FNRS through projects EQP n° 40021523 and EOS n°40007560 (PULSE), the ERC project HIGHRES and the Agence Nationale de la Recherche Scientifique – ANR through the project COMBY. C. Simon is a Research Fellow of the Fonds de la Recherche Scientifique – FNRS.

[1] P. Grelu and N. Akhmediev, Dissipative solitons for mode-locked lasers, *Nature Photonics* **6**, 84 (2012).

- [2] L. A. Lugiato and R. Lefever, Spatial Dissipative Structures in Passive Optical Systems, *Physical Review Letters* **58**, 2209 (1987).
- [3] F. Leo, S. Coen, P. Kockaert, S.-P. Gorza, P. Emplit, and M. Haelterman, Temporal cavity solitons in one-dimensional Kerr media as bits in an all-optical buffer, *Nature Photonics* **4**, 471 (2010).
- [4] T. Herr, V. Brasch, J. D. Jost, C. Y. Wang, N. M. Kondratiev, M. L. Gorodetsky, and T. J. Kippenberg, Temporal solitons in optical microresonators, *Nature Photonics* **8**, 145 (2014).
- [5] N. Englebort, F. De Lucia, P. Parra-Rivas, C. M. Arabi, P.-J. Sazio, S.-P. Gorza, and F. Leo, Parametrically driven Kerr cavity solitons, *Nature Photonics* **15**, 857 (2021).
- [6] T. Fortier and E. Baumann, 20 years of developments in optical frequency comb technology and applications, *Communications Physics* **2**, 153 (2019).
- [7] P. Marin-Palomo, J. N. Kemal, M. Karpov, A. Kordts, J. Pfeifle, M. H. P. Pfeiffer, P. Trocha, S. Wolf, V. Brasch, M. H. Anderson, R. Rosenberger, K. Vijayan, W. Freude, T. J. Kippenberg, and C. Koos, Microresonator-based solitons for massively parallel coherent optical communications, *Nature* **546**, 274 (2017).
- [8] J. Liu, E. Lucas, A. S. Raja, J. He, J. Riemensberger, R. N. Wang, M. Karpov, H. Guo, R. Bouchand, and T. J. Kippenberg, Photonic microwave generation in the X- and K-band using integrated soliton microcombs, *Nature Photonics* **14**, 486 (2020).
- [9] Z. L. Newman, V. Maurice, T. Drake, J. R. Stone, T. C. Briles, D. T. Spencer, C. Fredrick, Q. Li, D. Westly, B. R. Ilic, B. Shen, M.-G. Suh, K. Y. Yang, C. Johnson, D. M. S. Johnson, L. Hollberg, K. J. Vahala, K. Srinivasan, S. A. Diddams, J. Kitching, S. B. Papp, and M. T. Hummon, Architecture for the photonic integration of an optical atomic clock, *Optica* **6**, 680 (2019).
- [10] J. Riemensberger, A. Lukashchuk, M. Karpov, W. Weng, E. Lucas, J. Liu, and T. J. Kippenberg, Massively parallel coherent laser ranging using a soliton microcomb, *Nature* **581**, 164 (2020), number: 7807.
- [11] A. Kobyakov, M. Sauer, and D. Chowdhury, Stimulated Brillouin scattering in optical fibers, *Advances in Optics and Photonics* **2**, 1 (2010).
- [12] B. J. Eggleton, C. G. Poulton, P. T. Rakich, M. J. Steel, and G. Bahl, Brillouin integrated photonics, *Nature Photonics* **13**, 664 (2019).
- [13] A. Debut, S. Randoux, and J. Zemmouri, Linewidth narrowing in Brillouin lasers: Theoretical analysis, *Physical Review A* **62**, 023803 (2000).
- [14] J. Geng, S. Staines, Z. Wang, J. Zong, M. Blake, and S. Jiang, Highly stable low-noise Brillouin fiber laser with ultranarrow spectral linewidth, *IEEE Photonics Technology Letters* **18**, 1813 (2006).
- [15] J. Li, H. Lee, T. Chen, and K. J. Vahala, Characterization of a high coherence, Brillouin microcavity laser on silicon, *Optics Express* **20**, 20170 (2012).
- [16] S. Gundavarapu, G. M. Brodnik, M. Puckett, T. Huffman, D. Bose, R. Behunin, J. Wu, T. Qiu, C. Pinho, N. Chauhan, J. Nohava, P. T. Rakich, K. D. Nelson, M. Salit, and D. J. Blumenthal, Sub-hertz fundamental linewidth photonic integrated Brillouin laser, *Nature Photonics* **13**, 60 (2019).
- [17] W. Loh, S. Yegnanarayanan, F. O'Donnell, and P. W. Juodawlkis, Ultra-narrow linewidth Brillouin laser with

- nanokelvin temperature self-referencing, *Optica* **6**, 152 (2019).
- [18] F. Zarinetchi, S. P. Smith, and S. Ezekiel, Stimulated Brillouin fiber-optic laser gyroscope, *Optics Letters* **16**, 229 (1991).
- [19] J. Li, M.-G. Suh, and K. Vahala, Microresonator Brillouin gyroscope, *Optica* **4**, 346 (2017).
- [20] J. B. Murray, A. Cerjan, and B. Redding, Distributed Brillouin fiber laser sensor, *Optica* **9**, 80 (2022).
- [21] W. Loh, J. Stuart, D. Reens, C. D. Bruzewicz, D. Braje, J. Chiaverini, P. W. Juodawlkis, J. M. Sage, and R. McConnell, Operation of an optical atomic clock with a Brillouin laser subsystem, *Nature* **588**, 244 (2020).
- [22] J. Li, H. Lee, and K. J. Vahala, Microwave synthesizer using an on-chip Brillouin oscillator, *Nature Communications* **4**, 2097 (2013).
- [23] B. M. Heffernan, J. Greenberg, T. Hori, T. Tanigawa, and A. Rolland, Brillouin laser-driven terahertz oscillator up to 3 THz with femtosecond-level timing jitter, *Nature Photonics* **18**, 1263 (2024).
- [24] J. Tang, J. Sun, T. Chen, and Y. Zhou, A stable optical comb with double-Brillouin-frequency spacing assisted by multiple four-wave mixing processes, *Optical Fiber Technology* **17**, 608 (2011).
- [25] Q. Li, Z.-x. Jia, Z.-r. Li, Y.-d. Yang, J.-l. Xiao, S.-w. Chen, G.-s. Qin, Y.-z. Huang, and W.-p. Qin, Optical frequency combs generated by four-wave mixing in a dual wavelength Brillouin laser cavity, *AIP Advances* **7**, 075215 (2017).
- [26] E. Lucas, M. Deroh, and B. Kibler, Dynamic Interplay Between Kerr Combs and Brillouin Lasing in Fiber Cavities, *Laser & Photonics Reviews* **17**, 2300041 (2023).
- [27] M. Deroh, E. Lucas, and B. Kibler, Dispersion engineering in a Brillouin fiber laser cavity for Kerr frequency comb formation, *Optics Letters* **48**, 6388 (2023).
- [28] Y. Huang, Q. Li, J. Han, Z. Jia, Y. Yu, Y. Yang, J. Xiao, J. Wu, D. Zhang, Y. Huang, W. Qin, and G. Qin, Temporal soliton and optical frequency comb generation in a Brillouin laser cavity, *Optica* **6**, 1491 (2019).
- [29] D. Braje, L. Hollberg, and S. Diddams, Brillouin-Enhanced Hyperparametric Generation of an Optical Frequency Comb in a Monolithic Highly Nonlinear Fiber Cavity Pumped by a cw Laser, *Physical Review Letters* **102**, 193902 (2009).
- [30] T. F. S. Büttner, I. V. Kabakova, D. D. Hudson, R. Pant, C. G. Poulton, A. C. Judge, and B. J. Eggleton, Phase-locking and Pulse Generation in Multi-Frequency Brillouin Oscillator via Four Wave Mixing, *Scientific Reports* **4**, 5032 (2014), number: 1.
- [31] K. Jia, X. Wang, D. Kwon, J. Wang, E. Tsao, H. Liu, X. Ni, J. Guo, M. Yang, X. Jiang, J. Kim, S.-n. Zhu, Z. Xie, and S.-W. Huang, Photonic Flywheel in a Monolithic Fiber Resonator, *Physical Review Letters* **125**, 143902 (2020).
- [32] T. Bunel, J. Lumeau, A. Moreau, A. Fernandez, O. Llopis, G. Bourcier, A. M. Perego, M. Conforti, and A. Mussot, Brillouin-induced Kerr frequency comb in normal dispersion fiber Fabry Perot resonators, *Nature Communications* **16**, 5160 (2025).
- [33] Y. Bai, M. Zhang, Q. Shi, S. Ding, Y. Qin, Z. Xie, X. Jiang, and M. Xiao, Brillouin-Kerr Soliton Frequency Combs in an Optical Microresonator, *Physical Review Letters* **126**, 063901 (2021).
- [34] I. H. Do, D. Kim, D. Jeong, D. Suk, D. Kwon, J. Kim, J. H. Lee, and H. Lee, Self-stabilized soliton generation in a microresonator through mode-pulled Brillouin lasing, *Optics Letters* **46**, 1772 (2021).
- [35] H. Zhang, T. Tan, H.-J. Chen, Y. Yu, W. Wang, B. Chang, Y. Liang, Y. Guo, H. Zhou, H. Xia, Q. Gong, C. W. Wong, Y. Rao, Y.-F. Xiao, and B. Yao, Soliton Microcombs Multiplexing Using Intracavity-Stimulated Brillouin Lasers, *Physical Review Letters* **130**, 153802 (2023).
- [36] J. K. Jang, M. Erkintalo, S. G. Murdoch, and S. Coen, Ultraweak long-range interactions of solitons observed over astronomical distances, *Nature Photonics* **7**, 657 (2013).
- [37] Y. Wang, F. Leo, J. Fatome, M. Erkintalo, S. G. Murdoch, and S. Coen, Universal mechanism for the binding of temporal cavity solitons, *Optica* **4**, 855 (2017).
- [38] D. C. Cole, E. S. Lamb, P. Del'Haye, S. A. Diddams, and S. B. Papp, Soliton crystals in Kerr resonators, *Nature Photonics* **11**, 671 (2017).
- [39] W. Weng, R. Bouchand, E. Lucas, E. Obrzud, T. Herr, and T. J. Kippenberg, Heteronuclear soliton molecules in optical microresonators, *Nature Communications* **11**, 2402 (2020).
- [40] F. Amrani, M. Salhi, P. Grelu, H. Leblond, and F. Sanchez, Universal soliton pattern formations in passively mode-locked fiber lasers, *Optics Letters* **36**, 1545 (2011).
- [41] L. Nimmesgern, C. Beckh, H. Kempf, A. Leitenstorfer, and G. Herink, Soliton molecules in femtosecond fiber lasers: universal binding mechanism and direct electronic control, *Optica* **8**, 1334 (2021).
- [42] M. Dong and H. G. Winful, Unified approach to cascaded stimulated Brillouin scattering and frequency-comb generation, *Physical Review A* **93**, 043851 (2016).
- [43] D. A. Korobko, I. O. Zolotovskii, V. V. Svetukhin, A. V. Zhukov, A. N. Fomin, C. V. Borisova, and A. A. Fotiadi, Detuning effects in Brillouin ring microresonator laser, *Optics Express* **28**, 4962 (2020).
- [44] M. Erkintalo, K. Luo, J. K. Jang, S. Coen, and S. G. Murdoch, Bunching of temporal cavity solitons via forward Brillouin scattering, *New Journal of Physics* **17**, 115009 (2015).
- [45] M. Erkintalo, S. G. Murdoch, and S. Coen, Phase and intensity control of dissipative Kerr cavity solitons, *Journal of the Royal Society of New Zealand* **52**, 149 (2022).
- [46] T. Maggipinto, M. Brambilla, G. K. Harkness, and W. J. Firth, Cavity solitons in semiconductor microresonators: Existence, stability, and dynamical properties, *Physical Review E* **62**, 8726 (2000).
- [47] R. P. Millane and J. L. Eads, Diffraction by one-dimensional paracrystals and perturbed lattices, *Acta Crystallographica Section A Foundations of Crystallography* **56**, 497 (2000).
- [48] A. N. Pilipetskii, E. A. Golovchenko, and C. R. Menyuk, Acoustic effect in passively mode-locked fiber ring lasers, *Optics Letters* **20**, 907 (1995).
- [49] M. Conforti, T. Bunel, A. M. Perego, and A. Mussot, Fast and accurate modeling of Kerr-Brillouin combs in Fabry-Perot resonators, *Physical Review A* **112**, 033526 (2025).
- [50] S. Coen and M. Erkintalo, Universal scaling laws of Kerr frequency combs, *Optics Letters* **38**, 1790 (2013).

END MATTER

Theoretical model—Our theoretical analysis of the intracavity nonlinear dynamics, along with numerical simulations, relies on the following coupled mean-field equations:

$$T_r \frac{\partial \psi_{F/B}}{\partial t} = - \left(\frac{\Lambda}{2} + i\delta \right) \psi_{F/B} - i \frac{\beta_2 L}{2\beta_1^2} \frac{\partial^2 \psi_{F/B}}{\partial z^2} + \sqrt{\theta P_{\text{in}}^{F/B}} + i\gamma L (|\psi_{F/B}|^2 + 2\langle |\psi_{B/F}|^2 \rangle) \psi_{F/B} + i \frac{g_b}{2A_{\text{eff}}} \psi_{F/B} \otimes \left[\tilde{h}_b(\mp z) \times \left(\psi_{B/F}^* \otimes \psi_{B/F}(-z) \right) \right], \quad (\text{A1})$$

$$h_b(z) = \frac{\beta_1 \Omega_b \Gamma_b}{\sqrt{\Omega_b^2 - (\Gamma_b/2)^2}} \exp\left(-\frac{\Gamma_b}{2} \beta_1 z\right) \times \sin\left(\sqrt{\Omega_b^2 - (\Gamma_b/2)^2} \beta_1 z\right) u(z), \quad (\text{A2})$$

where t and z are the temporal and spatial coordinates in a reference frame moving at the light velocity in the cavity, and T_r is the round-trip time. $\psi_{F/B}$ are the envelopes of the forward (F) and backward (B) intracavity electric fields, with $|\psi_{F/B}|^2$ their powers. $u(z)$ is the Heaviside step function, $\langle a \rangle$ is the spatial average of the quantity a , \otimes is the spatial periodic convolution operator, and $\tilde{h}_b(z) = \sum_{n=-\infty}^{\infty} h_b(z - nL)$ is the periodic replication of the Brillouin response $h_b(z)$, with L the cavity length. $P_{\text{in}}^{F/B}$ are the input powers (note that only ψ_F is driven in the experiments, hence $P_{\text{in}}^B = 0$). δ is the detuning from the closest cavity resonance; $\beta_{1,2}$ are the inverse of the group velocity and group velocity dispersion, respectively; θ is the input coupling ratio, and γ is the nonlinear Kerr coefficient. The Brillouin gain is characterized by its strength g_b/A_{eff} , its bandwidth Γ_b , and the Stokes shift Ω_b . This set of equations is derived from the model presented in [49] for Fabry–Perot cavities, and adapted here to ring resonators where the forward and backward fields are distinct (see Supplemental Material). We note that since the FSR of our cavity (6.685 MHz) is several times smaller than the Brillouin bandwidth, $\Gamma_b/2\pi \approx 28$ MHz [11], $\tilde{h}_b(z)$ can be simplified to $h_b(z)$.

To theoretically analyze the interaction of a single (forward) CS with the backward wave S_1 , assuming single-mode backward Stokes lasing, we first note that the bandwidth of the forward gain induced by

$\psi_B = S_1 \exp(i\Omega_b \beta_1 z)$ is much narrower than the soliton spectrum (\sim THz). Consequently, the contribution of a single CS to ψ_F in the convolution term in Eq.(A1) can be approximated by a Dirac-delta function centered on the CS position z_{CS} and scaled by the integral of the (sech-shaped) soliton field $\pi\sqrt{P_{\text{CS}}\tau_{\text{CS}}}/\beta_1 \exp(i\phi_{\text{CS}})$, with P_{CS} , τ_{CS} , and ϕ_{CS} denoting the soliton peak power, duration, and phase, respectively. The Brillouin interaction term between S_1 and the CS in the equation of the forward wave thus reads $+i\Lambda\pi\sqrt{P_{\text{CS}}\tau_{\text{CS}}}/(2\beta_1^{-1}) \exp(i\phi_{\text{CS}}) \times h_b(z_{\text{CS}} - z) \exp[i\Omega_b\beta_1(z_{\text{CS}} - z)]$, in which we made the substitution corresponding to the lasing threshold of S_2 , which requires $g_b L |S_1|^2 / A_{\text{eff}} = \Lambda$ [at high detuning, the thresholds of the backward S_1 and forward S_2 Stokes waves are crossed simultaneously for increasing P_{in}^F in doubly resonant Brillouin lasers with $\Gamma_b \gg 2\pi \times \text{FSR}$ (see Supplemental Material Fig.S2(d))].

Experimental setup.—The experiments are performed in a ring resonator which consists of a standard optical fiber (SMF-28) looped on itself by a 99/1 coupler. The resulting low-loss cavity is 30.7 m-long and exhibits a round-trip loss of $\Lambda = 3.5\%$ (1% input coupling), corresponding to a finesse of $\mathcal{F} = 177$ (2.55×10^9 Q-factor). It is coherently driven by a narrow-linewidth continuous-wave laser at 1550.8 nm (see Supplemental Material for a detailed schematic of the experimental setup).

In the experiments, we either scan the laser frequency across the resonance or stabilize its detuning within the soliton region. For stabilization, we implement a dedicated scheme. We measure, on a logarithmic scale, the ratio between the optical powers in two adjacent frequency bands offset from the driving wavelength. This amounts to considering the slope of the soliton spectrum, uniquely determined by the linear cavity detuning [50]. The control thus does not require an additional laser signal and is independent of the number of stochastically generated cavity solitons. The long-term stability of the soliton pattern is studied by implementing an FPGA-based scheme in which the resonance is first scanned and, once CSs are detected, the dual-log stabilization loop engages to lock the detuning.

When the intracavity power increases, it eventually crosses the Brillouin laser threshold $g_b L P_{\text{cav}} / A_{\text{eff}} = \Lambda$. We measure an input threshold power at resonance $P_{\text{in}}^{\text{th}} \approx 300 \mu\text{W}$, which corresponds to $P_{\text{cav}}^{\text{th}} \approx 11.5 \text{ mW}$ and a Brillouin gain $g_b / A_{\text{eff}} = 0.10(3) \text{ W}^{-1} \text{ m}^{-1}$, in agreement with previous results in standard SMF fibers [11].

Supplementary information for: Self-organization of cavity solitons in Brillouin–Kerr ring resonators

Corentin Simon,¹ Matteo Conforti,² Loïc Van Bellinghen,¹ Maxime Fournier,¹ Arnaud Mussot,² François Leo,¹ and Simon-Pierre Gorza¹

¹*OPERA-photonics, Université libre de Bruxelles (U.L.B.),
50 Avenue F. D. Roosevelt, CP 194/5, B-1050 Brussels, Belgium*

²*University of Lille, CNRS, UMR 8523-PhLAM Physique des Lasers, Atomes et Molécules, F-59000, Lille, France*

(Dated: 5. March 2026)

This supplementary information is organized as follows. In the first section we give a detailed description of the experimental setup. In the second section we derive the mean-field equations describing the evolution of the counter-propagating optical fields in the ring resonator under the action of Kerr and Brillouin nonlinearities. In the third section, we describe the mechanism that couples soliton vacancies to the lattice distortion. In the fourth section, we provide a comparison of the threshold for CSs formation and Brillouin lasing. The set of parameters and the method used for the simulations are detailed in the fifth section. An additional figure at the end presents further simulations of the resonator’s nonlinear dynamics.

I. EXPERIMENTAL SETUP

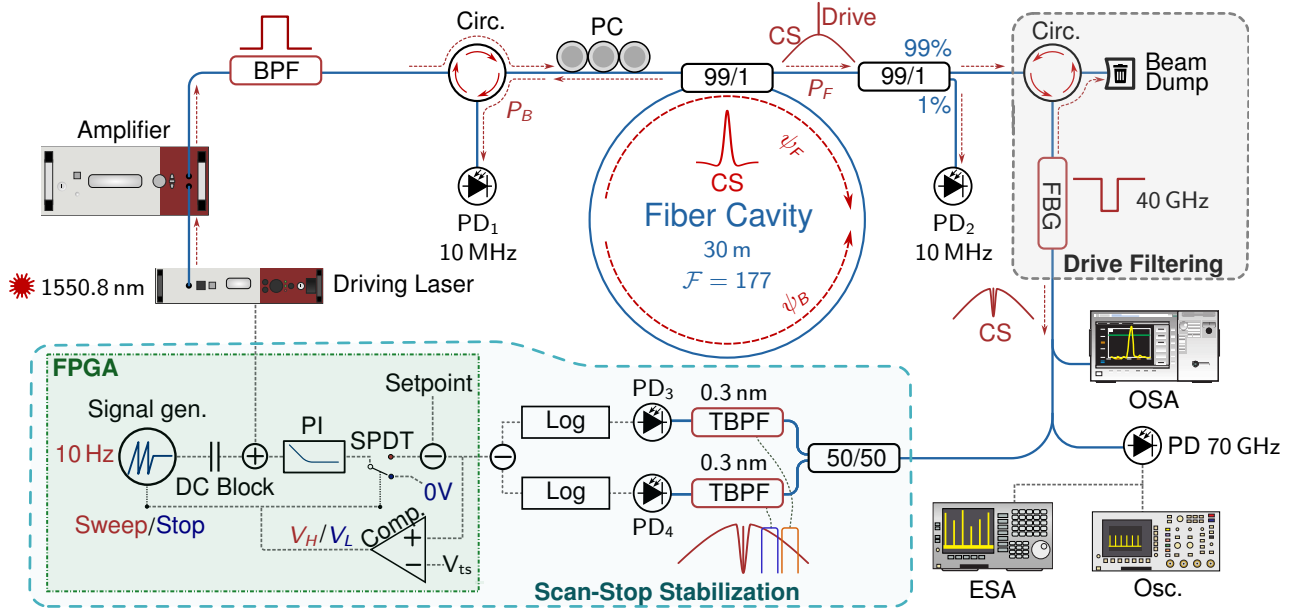


FIG. S1: Experimental set-up. Cavity solitons (CSs) and Brillouin lasing are generated in a ring cavity consisting of a fiber loop closed on itself and a 99/1 optical coupler. The driving beam is obtained from a continuous-wave laser (Driving laser), followed by an amplifier and a band-pass filter (BPF). The signal in the through port is filtered by a fiber Bragg grating (FBG). This signal is then sent either to measurement apparatuses or to the FPGA-based feedback loop for stabilization purposes. Circ., circulator, PC, polarization controller, TBPF (tunable band-pass filter), PD, photodiode, SPDT, single pole double throw switch, PI, proportional-integral controller, OSA, optical spectrum analyzer, Osc., oscilloscope, ESA, electric spectrum analyzer. ψ_F (ψ_B) forward (backward) intra-cavity field.

Experiments were performed in a ring cavity made of $L = 30.7$ m standard single-mode fiber [see Fig. (S1)]. The driving continuous-wave laser is a Koheras Adjustik at 1550.8 nm. A commercial amplifier (Koheras Boostik) is used to amplify the driving signal power. The amplified spontaneous emission (ASE) generated in the EDFA is suppressed by a narrow bandpass filter (100 GHz), centered on the driving laser wavelength. The driving beam is launched into the cavity through the coupler ($\theta \approx 1\%$) with a 600 mW input power. The polarization controller before the cavity

aligns the input polarization with one of the two cavity eigenmodes, while the first circulator separates the driving beam from the counterpropagating Brillouin laser signal. Its power is monitored by the first photodiode PD₁. The signal at the cavity through port is first split into two. The 1% tapped signal is used to measure the average power on a low-bandwidth photodiode (PD₂). The remaining part of the signal is then filtered by a narrowband fiber Bragg grating (40 GHz, 40 dB extinction ratio) to remove the driving frequency. Part of the filtered signal is sent to an optical spectrum analyzer and to a 70 GHz photodiode for time measurement on an oscilloscope (80 GHz bandwidth, 256 gigasamples per second) or to a radio-frequency spectrum analyzer.

The stabilization of the detuning between the driving laser and the cavity was performed by implementing a proportional-integral (PI) feedback loop to lock the laser frequency. A dedicated dual-logarithmic detection scheme generates the error signal. This signal is based on the logarithm of the ratio of the optical powers measured by PD3 and PD4 in two adjacent filtered frequency bands. This is equivalent to measuring the slope of the soliton spectrum on a logarithmic scale, which is solely determined by the cavity detuning [1]. The resulting control signal thus enables detuning stabilization while remaining independent of the number of CSs, contrary to schemes based on a single frequency filter [2].

To determine the Brillouin gain (i.e. g_b/A_{eff}) of our optical fiber, we measured the Brillouin lasing threshold input power P_b^{th} of our cavity. To this end, we used a PDH locking scheme to drive the cavity on resonance, and we progressively increased the input power until a backward signal is detected. Taking into account the phase modulation of the driving laser for the PDH locking, the Brillouin gain is given by:

$$(g_b/A_{\text{eff}})^{-1} = \mathcal{F}^3 \theta P_b^{\text{th}} L / (2\pi^3) \times J_0(\pi V_{\text{PDH}}/V_\pi)^2, \quad (\text{S1})$$

where $\mathcal{F} = 2\pi/\Lambda$ is the cavity finesse, J_0 denotes the Bessel function of the first kind, and V_{PDH} , V_π are the amplitude of the voltage signal sent to the modulator and the V_π voltage of the modulator, respectively. We used $V_{\text{PDH}} = 0.5$ V and $V_\pi = 5(1)$ V (we note that this leads to a reduction of the driving power of 4.5% compared to the unmodulated case). We measured $P_b^{\text{th}} = 300(60)$ μW . Thus, taking into account the values of the other parameters and their uncertainties: $\theta = 0.013(3)$ and $\mathcal{F} = 177(3)$, a Brillouin gain value of $g_b = 0.10(3)$ $\text{W}^{-1} \text{m}^{-1}$ is obtained.

II. DERIVATION OF THE MEAN-FIELD MODEL

The evolution equations for the slowly varying forward (clockwise) $F(z, t)$ and backward (counterclockwise) $B(z, t)$ optical fields, and the acoustic wave Q read as [3–6]:

$$\frac{\partial F}{\partial z} + \beta_1 \frac{\partial F}{\partial t} + i \frac{\beta_2}{2} \frac{\partial^2 F}{\partial t^2} = i\gamma (|F|^2 + X|B|^2) F + \frac{g_b}{2A_{\text{eff}}} QB, \quad (\text{S2})$$

$$-\frac{\partial B}{\partial z} + \beta_1 \frac{\partial B}{\partial t} + i \frac{\beta_2}{2} \frac{\partial^2 B}{\partial t^2} = i\gamma (|B|^2 + X|F|^2) B - \frac{g_b}{2A_{\text{eff}}} Q^* F, \quad (\text{S3})$$

$$\left(\frac{\partial^2}{\partial t^2} + \Gamma_b \frac{\partial}{\partial t} + \Omega_b^2 \right) Q = i\Omega_b \Gamma_b F B^*, \quad (\text{S4})$$

where $v_g = \beta_1^{-1}$ is the group velocity, β_2 the group velocity dispersion (GVD), and γ the waveguide nonlinear coefficient ($\text{m}^{-1}\text{W}^{-1}$). The parameter X describes the cross-phase modulation (XPM) and is taken to be $X = 2$. The Brillouin gain is g_b (m/W), A_{eff} is the effective area of the mode, $\tau_b = 1/\Gamma_b$ is the phonon lifetime and Ω_b is the Brillouin shift. The optical fields are normalized in such a way that their square modulus gives the instantaneous power.

Assuming a ring resonator and external coherent driving, the propagation equations (S2,S3) are complemented with the following boundary conditions at the coupler, which connect the beginning ($z = 0$) and the end ($z = L$) of the resonator:

$$F(0, t) = \mathcal{T} E_{\text{in}} + \mathcal{R} e^{-i\delta} F(L, t), \quad (\text{S5})$$

$$B(L, t) = \mathcal{T} E_{\text{in}}^B + \mathcal{R} e^{-i\delta} B(0, t), \quad (\text{S6})$$

where $\delta = 2\pi m_0 - \phi_0$ is the phase detuning between the driving fields ($E_{\text{in}}, E_{\text{in}}^B$) and the closest resonance indexed by the integer m_0 (assumed here identical for both propagation directions for simplicity). The phase ϕ_0 accounts for the phase acquired during propagation over the resonator length L ($\beta_0 L$, with β_0 the propagation constant of the mode), and any possible contribution from the coupler. The coupler transmission and reflection coefficients in amplitude are \mathcal{T} and \mathcal{R} , respectively.

To develop a mean-field description from Eqs.(S2-S6), we adapt the method recently introduced for Fabry-Perot cavities (FP) [3] to ring resonators. The procedure can be summarized in four steps: (i) perform a change of variables for enforcing spatial periodic boundary conditions to properly define the cavity modes; (ii) simplify the propagation equations for the transformed fields through the good-cavity approximation; (iii) find the coupled equations for the cavity modes; and (iv) derive a partial differential equation ruling the mean-fields in each direction. These are defined as the sum of the cavity modes with slowly time-varying amplitudes.

The appropriate change of variables turns out to be [7]:

$$f(z, t) = e^{\frac{z}{L}(\ln \mathcal{R} - i\delta)} F(z, t) + \mathcal{T} \frac{z}{L} E_{\text{in}}, \quad (\text{S7})$$

$$b(z, t) = e^{\frac{L-z}{L}(\ln \mathcal{R} - i\delta)} B(z, t) + \mathcal{T} \frac{L-z}{L} E_{\text{in}}^B. \quad (\text{S8})$$

From Eqs. (S5,S6), we obtain periodic boundary conditions for the new variables:

$$f(0, t) = f(L, t), \quad (\text{S9})$$

$$b(0, t) = b(L, t). \quad (\text{S10})$$

We now restrict our analysis to good cavities by assuming $\mathcal{R} \rightarrow 1$, $\mathcal{T} \rightarrow 0$, $\delta \rightarrow 0$. At zero-th order we have $F \approx f$ and $B \approx b$. From Eqs. (S7-S8), we compute $\partial_z F$, $\partial_t F$, $\partial_z B$, $\partial_t B$ as a function of f, b and their derivatives. We truncate the resulting expressions at first order in \mathcal{T} , $(1 - \mathcal{R})$ and δ and insert them into Eqs. (S2,S3). By considering that dispersion and nonlinearity are first-order corrections, we may use zero-order expansions in the dispersive and nonlinear terms. These approximations greatly simplify the propagation equations, which then read:

$$\frac{\partial f}{\partial z} - \frac{\mathcal{T}}{L} E_{\text{in}} - \left(\frac{\ln \mathcal{R}}{L} - i \frac{\delta}{L} \right) f + \beta_1 \frac{\partial f}{\partial t} + i \frac{\beta_2}{2} \frac{\partial^2 f}{\partial t^2} = i\gamma (|f|^2 + X|b|^2) f + \frac{g_b}{2A_{\text{eff}}} Qb, \quad (\text{S11})$$

$$-\frac{\partial b}{\partial z} - \frac{\mathcal{T}}{L} E_{\text{in}}^B - \left(\frac{\ln \mathcal{R}}{L} - i \frac{\delta}{L} \right) b + \beta_1 \frac{\partial b}{\partial t} + i \frac{\beta_2}{2} \frac{\partial^2 b}{\partial t^2} = i\gamma (|b|^2 + X|f|^2) b - \frac{g_b}{2A_{\text{eff}}} Q^* f. \quad (\text{S12})$$

The modes of the lossless, empty and undriven cavity [$\beta_2 = \delta = \gamma = E_{\text{in}} = E_{\text{in}}^B = g_b = 0$, $\mathcal{R} = 1$] can be written as:

$$f_m(z, t) = a_m e^{-i\omega_m t} e^{ik_m z} = a_m e^{-i\omega_m(t - \beta_1 z)}, \quad (\text{S13})$$

$$b_m(z, t) = b_m e^{-i\omega_m t} e^{-ik_m z} = b_m e^{-i\omega_m(t + \beta_1 z)}, \quad (\text{S14})$$

where the frequency and wavenumber are:

$$\omega_m = \frac{2\pi}{\beta_1 L} m, \quad k_m = \beta_1 \omega_m = \frac{2\pi}{L} m. \quad (\text{S15})$$

We have two families of modes with independent amplitudes for the two propagation directions. This is the main difference from FP resonators, where the amplitudes of forward and backward modes are identical [8]. We thus separately write the fields in Eqs. (S11,S12) as the sum of the modes, allowing for a temporal variation of the modal amplitudes:

$$f(z, t) = \sum_m a_m(t) e^{-i\omega_m(t - \beta_1 z)}, \quad (\text{S16})$$

$$b(z, t) = \sum_m b_m(t) e^{-i\omega_m(t + \beta_1 z)}. \quad (\text{S17})$$

To obtain the evolution of the amplitudes $a_m(t)$, we first apply the expansions Eqs. (S16,S17) in Eq. (S11). The result is then projected onto each forward mode by multiplying the equation by $\frac{1}{L} \exp[i\omega_n(t - \beta_1 z)]$, and integrating from $z = 0$ to $z = L$. After some algebra, we obtain:

$$\beta_1 \dot{a}_n - \left(\frac{\ln \mathcal{R}}{L} - i \frac{\delta}{L} \right) a_n + i \frac{\beta_2}{2} (\ddot{a}_n - 2i\omega_n \dot{a}_n - \omega_n^2 a_n) - \frac{\mathcal{T}}{L} E_{\text{in}} \delta_{n0} = i\gamma \mathcal{K}_n^f + \frac{g_b}{2A_{\text{eff}}} \mathcal{B}_n^f, \quad (\text{S18})$$

where, δ_{n0} is the Kronecker delta. Similarly, the evolution of $b_m(t)$ is obtained from Eq.(S12), through the projection onto the backward modes (multiplication by $\frac{1}{L} \exp[i\omega_n(t + \beta_1 z)]$):

$$\beta_1 \dot{b}_n - \left(\frac{\ln \mathcal{R}}{L} - i \frac{\delta}{L} \right) b_n + i \frac{\beta_2}{2} (\ddot{b}_n - 2i\omega_n \dot{b}_n - \omega_n^2 b_n) - \frac{\mathcal{T}}{L} E_{\text{in}}^B \delta_{n0} = i\gamma \mathcal{K}_n^b - \frac{g_b}{2A_{\text{eff}}} \mathcal{B}_n^b. \quad (\text{S19})$$

In these equations, $\mathcal{K}_n^{f/b}$ and $\mathcal{B}_n^{f/b}$ are the nonlinear forward or backward Kerr and Brillouin coefficients. They are defined as follow.

- **Kerr term**

The Kerr terms for the forward and backward fields are:

$$\mathcal{K}_n^f = \frac{1}{L} \int_0^L (|f|^2 + X|b|^2) f e^{i\omega_n(t - \beta_1 z)} dz = \sum_{n', n''} a_{n'} a_{n''}^* a_{n - n' + n''} + X \sum_{n', n''} b_{n'} b_{n''}^* a_{n + n' - n''} e^{-i2(\omega_{n'} - \omega_{n''})t}, \quad (\text{S20})$$

$$\mathcal{K}_n^b = \frac{1}{L} \int_0^L (|b|^2 + X|f|^2) b e^{i\omega_n(t + \beta_1 z)} dz = \sum_{n', n''} b_{n'} b_{n''}^* b_{n - n' + n''} + X \sum_{n', n''} a_{n'} a_{n''}^* b_{n + n' - n''} e^{-i2(\omega_{n'} - \omega_{n''})t}. \quad (\text{S21})$$

- **Brillouin term**

The strategy is to find an expression for the acoustic wave Q as a function of the modal amplitudes of the optical fields. To this end, we first decompose the acoustic wave by expanding it over the cavity modes, while keeping the temporal dependence general:

$$Q(z, t) = \sum_m Q_m(t) e^{ik_m z}. \quad (\text{S22})$$

We then insert Eq. (S22) in Eq. (S4), and expand the nonlinear term over the modes. Separating the terms oscillating with the same wavenumber we obtain:

$$\left(\frac{\partial^2}{\partial t^2} + \Gamma_b \frac{\partial}{\partial t} + \Omega_b^2\right) Q_m(t) = i\Gamma_b \Omega_b \sum_n a_n b_{m-n}^* e^{-i(2\omega_n - \omega_m)t}. \quad (\text{S23})$$

Equation (S23) is a set of forced harmonic oscillators, whose steady-state solutions can be written as

$$Q_m(t) = \sum_p q_{mp}(t) e^{-i\Omega_p t}. \quad (\text{S24})$$

We substitute Eq.(S24) into Eq.(S23) and assume that $q_{mp}(t)$ varies slowly with respect to Ω_p . By collecting all terms with identical oscillation frequencies, we get $\Omega_p = 2\omega_n - \omega_m$ and

$$q_{m,2n-m} = iH_b(2\omega_n - \omega_m) a_n b_{m-n}^*, \quad (\text{S25})$$

where we have defined the Brillouin response in the frequency domain as:

$$H_b(\omega_n) = \frac{\Omega_b \Gamma_b}{\Omega_b^2 - \omega_n^2 - i\omega_n \Gamma_b}. \quad (\text{S26})$$

The acoustic wave envelope has thus the following expression:

$$Q(z, t) = i \sum_{n,m} a_n b_{m-n}^* H_b(2\omega_n - \omega_m) e^{-i(2\omega_n - \omega_m)t} e^{ik_m z}. \quad (\text{S27})$$

Finally, as for the Kerr terms, the forward Brillouin term $\propto Qb$ in Eq. (S11) is first expanded over the cavity modes and then projected onto each forward mode. It follows the Brillouin coefficients:

$$\mathcal{B}_n^f = \frac{1}{L} \int_0^L Q b e^{i\omega_n(t - \beta_1 z)} dz = i \sum_{n', n''} a_{n'} b_{n''} b_{n-n'+n''}^* H_b(2\omega_{n'} - \omega_{n''} - \omega_n) e^{-i(2\omega_{n'} - \omega_n)t}. \quad (\text{S28})$$

Similarly, for the backward field, we have:

$$\mathcal{B}_n^b = \frac{1}{L} \int_0^L Q^* f e^{i\omega_n(t + \beta_1 z)} dz = -i \sum_{n', n''} a_{n'}^* a_{n''} b_{n-n'+n''} H_b^*(2\omega_{n'} - \omega_{n''} - \omega_n) e^{2i(\omega_{n'} - \omega_n)t}. \quad (\text{S29})$$

We note that since $H_b(\omega) = H_b^*(-\omega)$, it is straightforward to show, via an appropriate change of indices, that $\mathcal{B}_n^b(a_{n'}, b_{n''}) = -\mathcal{B}_n^f(b_{n'}, a_{n''})$.

To obtain the coupled equations for the cavity modes, we insert the nonlinear terms Eqs.(S28,S29) in Eqs.(S18,S19). We then make use of the assumption that the modal amplitudes change slowly over a round-trip (i.e. $|\dot{a}_n| \ll |\omega_n a_n|$) to simplify the dispersive contribution and to average out the fast oscillations in the nonlinear terms. It follows:

$$\begin{aligned} \dot{a}_n + \left(\kappa + i\frac{\delta}{\beta_1 L} - i\frac{\beta_2}{2\beta_1} \omega_n^2\right) a_n - \frac{\mathcal{T}}{\beta_1 L} E_{\text{in}} \delta_{n0} &= i\frac{\gamma}{\beta_1} \left(\sum_{n', n''} a_{n'} a_{n''}^* a_{n-n'+n''} + X a_n \sum_{n'} |b_{n'}|^2 \right) \\ &+ i\frac{g_b}{2A_{\text{eff}} \beta_1} a_n \sum_{n'} |b_{n'}|^2 H_b(\omega_n - \omega_{n'}), \end{aligned} \quad (\text{S30})$$

$$\begin{aligned} \dot{b}_n + \left(\kappa + i\frac{\delta}{\beta_1 L} - i\frac{\beta_2}{2\beta_1} \omega_n^2\right) b_n - \frac{\mathcal{T}}{\beta_1 L} E_{\text{in}}^B \delta_{n0} &= i\frac{\gamma}{\beta_1} \left(\sum_{n', n''} b_{n'} b_{n''}^* b_{n-n'+n''} + X b_n \sum_{n'} |a_{n'}|^2 \right) \\ &+ i\frac{g_b}{2A_{\text{eff}} \beta_1} b_n \sum_{n'} |a_{n'}|^2 H_b(\omega_n - \omega_{n'}), \end{aligned} \quad (\text{S31})$$

where we have defined the decay rate $\kappa = -\frac{\ln \mathcal{R}}{\beta_1 L}$. Equations (S30,S31) describe the temporal evolution of the slowly varying amplitudes of forward and backward modes. They constitute the coupled-mode description commonly used

for micro-resonators. It is easy to give a physical interpretation of the Brillouin term in these equations. The complex gain experienced by the mode a_n (respectively b_n) is given by the discrete convolution of the power spectrum of the counter-propagating wave $|b_m|^2$ (respectively $|a_n|^2$) and the Brillouin response $H_b(\omega_m)$.

As a final step, we derive the equivalent model for slowly varying envelopes of the forward and backward fields [9], defined as follows:

$$\psi_F(z, t) = \sum_m a_m(t) e^{ik_m z}, \quad \psi_B(z, t) = \sum_m b_m(t) e^{-ik_m z}. \quad (\text{S32})$$

These fields are periodic with period L ($k_m = 2\pi m/L = \beta_1 \omega_m$), and the modal amplitudes can be retrieved as follows:

$$a_m(t) = \frac{1}{L} \int_0^L \psi_F(z, t) e^{-ik_m z} dz, \quad b_m(t) = \frac{1}{L} \int_0^L \psi_B(z, t) e^{ik_m z} dz. \quad (\text{S33})$$

Multiplying Eq.(S30) by $e^{i\beta_1 \omega_m z}$ and Eq.(S31) by $e^{-i\beta_1 \omega_m z}$, summing over m , and using

$$\frac{\partial \psi_F}{\partial t} = \sum_m \dot{a}_m(t) e^{i\beta_1 \omega_m z}, \quad \frac{\partial^n \psi_F}{\partial z^n} = \sum_m (i\beta_1 \omega_m)^n a_m(t) e^{i\beta_1 \omega_m z},$$

as well as the analogous relations for $\partial_t \psi_B$ and $\partial_z^n \psi_B$, Eq.(1) of the main manuscript is finally obtained:

$$\begin{aligned} T_r \frac{\partial \psi_{F/B}}{\partial t} = & - \left(\frac{\Lambda}{2} + i\delta \right) \psi_{F/B} - i \frac{\beta_2 L}{2\beta_1^2} \frac{\partial^2 \psi_{F/B}}{\partial z^2} + \sqrt{\theta P_{\text{in}}^{F/B}} + i\gamma L (|\psi_{F/B}|^2 + 2\langle |\psi_{B/F}|^2 \rangle) \psi_{F/B} \\ & + i \frac{g_b}{2A_{\text{eff}}} \psi_{F/B} \otimes \left[\tilde{h}_b(\mp z) \cdot \left(\psi_{B/F}^* \otimes \psi_{B/F}(-z) \right) \right], \quad (\text{S34}) \end{aligned}$$

where $\langle \cdot \rangle = \frac{1}{2} \int_0^L (\cdot) dz$ denotes spatial average, $T_r = \beta_1 L$ and $\frac{\Lambda}{2} = \kappa T_r \approx 1 - \mathcal{R}$, $\mathcal{T}E_{\text{in}}^{F,B} = \sqrt{\theta P_{\text{in}}^{F/B}}$. In this equation, we have defined the (periodic) convolution as

$$[\psi \otimes \tilde{h}_b](z) = \int_0^L \psi(\xi, t) \tilde{h}_b(z - \xi) d\xi, \quad (\text{S35})$$

and the Brillouin response in the *spatial* domain as:

$$\tilde{h}_b(z) = \sum_n \frac{H_b(\omega_n)}{L} e^{-ik_n z}. \quad (\text{S36})$$

Equation (S36) describes the Brillouin response in the spatial domain as an L -periodic function of z , where the Fourier coefficients are $h_n = H_b(\omega_n)/L$. From the properties of Fourier series, we note that $\tilde{h}_b(z) = \sum_n h(z - nL)$ is the periodic replication of the inverse Fourier transform in z of the Brillouin response (thus written as a function of the wavenumber):

$$H_b(k/\beta_1) = \frac{\Omega_b \Gamma_b}{\Omega_b^2 - (k/\beta_1)^2 - i\Gamma_b k/\beta_1} = \int_{-\infty}^{\infty} h(z) e^{ikz} dz \quad (\text{S37})$$

$$h(z) = \frac{\beta_1 \Omega_b \Gamma_b}{\sqrt{\Omega_b^2 - (\Gamma_b/2)^2}} e^{-\frac{\Gamma_b}{2} \beta_1 z} \sin \left(\sqrt{\Omega_b^2 - (\Gamma_b/2)^2} \beta_1 z \right) u(z), \quad (\text{S38})$$

where $u(z)$ is the Heaviside step function.

III. CSS EQUILIBRIUM POSITIONS AND IMPACT OF A VACANCY

We derive how a vacancy in the soliton lattice induces a distortion in each subsequent CS. To this end, we begin by introducing the interaction potential generated by a single CS, which is of the form (motivated by the experimental fit and numerical computation):

$$d(\tau) = \sin(a\tau + \Delta\phi) \exp(-c\tau)u(\tau). \quad (\text{S39})$$

Here $\tau = -\beta_1 z$ denotes the cavity fast time, a the oscillation frequency of the interaction ($\approx 2\Omega_b$) and $c \approx \Gamma_b/2$ its damping rate. $u(\tau)$ is the Heaviside function which ensures causality. In what follows, we neglect the periodic boundary condition, assuming that the cavity round-trip time is much longer than the lifetime of the acoustic wave.

For a single CS, the potential creates a lattice with period $p = 2\pi/a$, within which subsequent solitons can be trapped. Each trapped CS, in turn, contributes to the total interaction potential, so that any given soliton experiences the cumulative effect of all preceding CSs. We consider the total interaction potential in the vicinity of the n -th lattice site, denoted $V_n(\tau)$ and valid for $|\tau - np| \lesssim p$. Owing to the common oscillation frequency of all contributions, we assume that this cumulative potential has the same functional form:

$$V_n(\tau) = \sum_{i|\tau_i < np}^{\text{CS}} d(\tau - \tau_i) = A_n \sin(a\tau + \phi_n) \exp(-c(\tau - np)). \quad (\text{S40})$$

The trapping position of a possible CS is

$$\tau_n = np - \phi_n/a \quad (\text{S41})$$

where we neglect the weak correction arising from the decaying exponential envelope. The presence or absence of a vacancy in the lattice will affect the position of subsequent CSs in distinct ways.

Occupied n^{th} site

If a CS is present, its individual contribution to the potential will modify the potential around the next lattice point $n + 1$:

$$\begin{aligned} V_{n+1} &= V_n + d(\tau - \tau_n) \\ &= \exp(-c(\tau - (n+1)p)) \times [A_n \sin(a\tau + \phi_n) \exp(-cp) + \sin(a\tau + \Delta\phi + \phi_n) \exp(-c\Delta_n)] \\ &= \exp(-c(\tau - (n+1)p)) A_{n+1} \sin(a\tau + \phi_{n+1}). \end{aligned} \quad (\text{S42})$$

For convenience, we introduce $\Delta_n = (n+1)p - \tau_n$ and $\xi_n = \exp(-c(\Delta_n - p))/A_n \approx 1/A_n$, where the latter approximation holds for $\Delta_n \approx p$ and sufficiently large A_n , such that $\xi_n \ll 1$, so that the additional contribution of a single soliton constitutes a small perturbation.

Using trigonometric addition formulas, we obtain

$$A_{n+1} = A_n \exp(-cp) \sqrt{(1 + \xi_n \cos \Delta\phi)^2 + (\xi_n \sin \Delta\phi)^2} \quad (\text{S43})$$

$$\begin{aligned} \phi_{n+1} &= \tan^{-1} \frac{\sin(\phi_n) + \xi_n \sin(\Delta\phi + \phi_n)}{\cos(\phi_n) + \xi_n \cos(\Delta\phi + \phi_n)} \\ &= \phi_n + \xi_n \sin \Delta\phi + \mathcal{O}(\xi_n^2) \end{aligned} \quad (\text{S44})$$

To first order in ξ_n , the phase therefore undergoes a constant increment proportional to $\sin(\Delta\phi)$. Since the trapping position depends on ϕ_n , the position of the subsequent CS is shifted by:

$$\delta\tau_{n+1} = -\frac{\xi_n \sin \Delta\phi}{a}. \quad (\text{S45})$$

Fully occupied lattice

We now consider a fully occupied lattice. Translational invariance requires $A_{n+1} = A_n$, which yields the self-consistency condition

$$\begin{aligned}\xi_n = \xi &= -\cos(\Delta\phi) + \sqrt{\cos(\Delta\phi)^2 + \exp(2cp) - 1} \\ &\approx -\cos(\Delta\phi) + \sqrt{\cos(\Delta\phi)^2 + 2cp},\end{aligned}\tag{S46}$$

where we used $\exp(2cp) \approx 1 + 2cp$ for $cp \approx \pi\Gamma_b/(2\Omega_b) \ll 1$. Since ξ_n is now constant, the phase increment becomes

$$\phi_{n+1} - \phi_n = \xi \sin(\Delta\phi)\tag{S47}$$

corresponding to a uniform renormalization of the lattice spacing. The effective period is therefore

$$p' = \frac{p}{1 + \xi \sin(\Delta\phi)/2\pi}\tag{S48}$$

Unoccupied n^{th} site

If a vacancy occurs now at position n , the additional contribution $d(\tau - \tau_n)$ is absent. Consequently,

$$\begin{aligned}V_{n+1} &= V_n \\ \phi_{n+1} &= \phi_n \\ A_{n+1} &= \exp(-cp)A_n.\end{aligned}$$

Compared to the fully occupied case, this corresponds to a missing phase shift $\xi \sin(\Delta\phi)$. All subsequent lattice points are therefore shifted by:

$$\delta\tau_{n+1} = \frac{\xi \sin \Delta\phi}{a}.\tag{S49}$$

A vacancy thus acts as a localized defect whose effect propagates to all following soliton positions, thereby mediating a long-range coupling between lattice occupancy and positional distortion.

Finite lattice Segment

For a fully occupied lattice segment surrounded by vacancies, the inter-soliton delay changes monotonically as it evolves from p to p' . This smooth variation reflects the gradual buildup of the phase increment $\phi_{n+1} - \phi_n$ from zero (empty lattice) to its asymptotic constant value in the bulk lattice. This variation is reflected in the phase of the time oscillation of CSs due to the S_0 - S_2 beat signal. Specifically, one expects a pronounced curvature at the onset of the fully occupied segment, asymptotically evolving to a constant slope. This explains the pattern seen in Fig. 4(b) of the main paper for $-10 \text{ ns} < \tau < -5 \text{ ns}$.

Finally, we note that the periodic boundary conditions of the cavity may introduce a small collective drift of the entire soliton ensemble, as the total accumulated phase must remain compatible with cavity periodicity. Although this global constraint was included when fitting the interaction potential, it does not alter the local vacancy-induced distortion mechanism described above.

IV. BRILLOUIN AND CS THRESHOLDS

We first compare the input power threshold of the first Brillouin order S_1 ($P_b^{th,1}$) with the minimum power (P_{CS}) to drive a CS. The Brillouin lasing threshold depends on the intra-cavity power and thus on the cavity detuning δ . Assuming that the Brillouin gain peaks at the frequency of a cavity mode, it is given by:

$$\frac{g_b}{A_{\text{eff}}} L \frac{\theta P_b^{th,1}}{\Lambda^2/4 + 4(1 - \Lambda/2) \sin(\delta/2)^2} = \Lambda. \quad (\text{S50})$$

For CSs, the minimum driving power at a given detuning is determined by the saddle-node bifurcation (SN_{CS}) that marks the end of the soliton existence range. Without Brillouin interaction it is given by:

$$\delta < \frac{\pi^2 \theta P_{CS} \gamma L}{2 \Lambda^2}. \quad (\text{S51})$$

The CS and Brillouin thresholds are strongly dependent on the cavity loss Λ as shown in Figs. S2(a-c), where the three possible regimes are identified: Brillouin lasing alone, Brillouin-less cavity solitons, and the coexistence of Brillouin and CSs. Because the intra-cavity power reaches a minimum at $\delta = \pi$, there exists a loss threshold above which CSs cannot form without Brillouin lasing. Conversely, in low-loss resonators, this regime becomes accessible at large detunings and low driving powers. As seen in Fig. S2(b), we operated the cavity in the coexistence region.

It is also instructive to examine the driving power required to reach the successive thresholds of the higher-order Stokes waves S_j ($j > 1$). Above each threshold, the oscillation condition imposes $P_{S_{j-1}} - P_{S_{j+1}} = \Lambda A_{\text{eff}} / (g_b L)$. As a consequence, at large detunings, as in the experiments, the Brillouin orders emerge in pairs, [S_{2n+1} and S_{2n+2} , see Fig. S2(d)], with a small hysteresis. This analysis shows that, in the absence of any influence of the CSs on the Brillouin thresholds, four thresholds should be crossed in the experiments. Numerical simulations without CSs confirm this expectation [see Fig. S3(e)]. However, the experiments only exhibit the first two Stokes waves [see Figs. 3 (b-c) of the main manuscript]. Simulations based on the mean-field model reveal that this discrepancy arises from the large number of CSs circulating in the cavity [Fig. S3(d)]. The CSs modify the intracavity spectral power at the driven frequency (S_0), thereby increasing the input power required to reach the Brillouin thresholds.

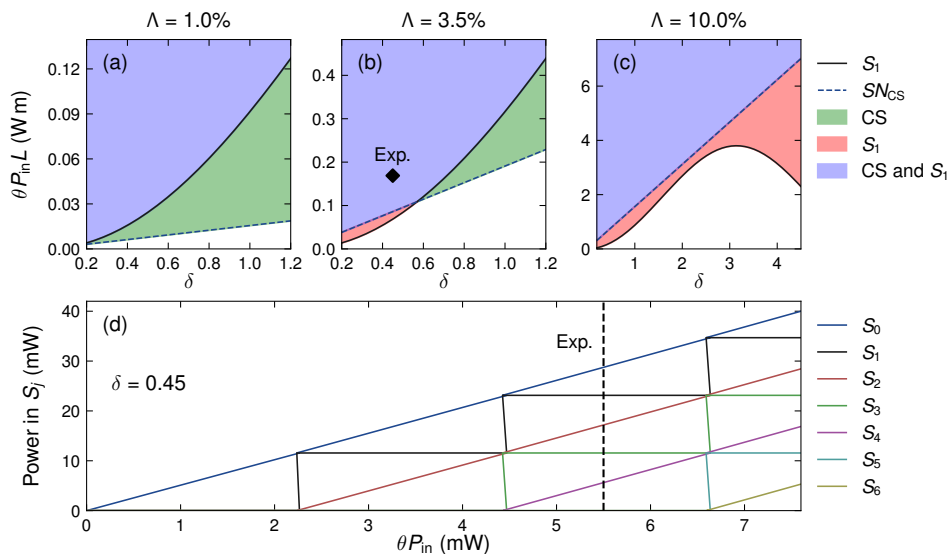


FIG. S2: (a)-(c) First-order Brillouin threshold (S_1), $P_{in} = P_b^{th,1}$, and CS threshold (SN_{CS}), $P_{in} = P_{CS}$, for different cavity loss Λ . The shaded areas distinguish the different regimes: CS, only cavity solitons, S_1 Brillouin lasing only, CS and S_1 coexistence of soliton with Brillouin lasing. (d) Input pump power thresholds for the formation of the j -th Stokes wave S_j in the resonator at $\delta = 0.45$ and $\Lambda = 3.5\%$. The diamond in (c) and the vertical line in (d) represent the experimental conditions.

V. SIMULATION PARAMETERS AND SIMULATION METHOD

Simulation parameters—The simulation parameters are given in Table S1. We selected the set of parameters that provides the best agreement between the numerical and experimental results. This explains the small discrepancies with the experimental values for the input coupler and driving power ($\theta = 1.3\%$ from the datasheet and $P_{\text{in}} = 600$ mW in the experiment). We note that this choice of simulation parameters is not unique, as several nearby combinations of γ , θ , α , and P_{in} can reproduce the same observed dynamics. We further note that the actual values of the fiber and component parameters are subject to uncertainties, and that parasitic effects, such as time-varying polarization-dependent loss (PDL), might slightly modify the cavity loss experienced by the driven modes (Λ) between the characterization stage and the actual experiments.

In simulations, a small amount of white noise P_{noise} was added to the cavity field at each roundtrip to mimic the residual drive ASE floor and to seed the Brillouin lasing. The value of P_{noise} is somewhat arbitrary and does not significantly affect the simulation outcomes.

Simulation method—A 5(6) adaptive Runge-Kutta method in the Interaction Picture (RKIP) [10] was used to numerically solve the coupled equations. We stress that due to the counter-propagating nature of the fields, the simulation window must encompass the entire cavity round-trip time (≈ 150 ns). This requirement is computationally expensive. To address this challenge, the inherent parallelism of these equations was leveraged to implement the simulation on a GPU, resulting in a speed-up factor of 10 to 100, depending on the hardware. For example, simulating 4000 roundtrips requires approximately 3 min on an NVIDIA RTX 4080 for 2×2^{19} simulation points.

| Parameter | Value | Unit |
|----------------------------------------|------------------------|-------------------------------|
| β_1 | 4.87×10^{-9} | s m^{-1} |
| β_2 | -2.1×10^{-26} | $\text{s}^2 \text{m}^{-1}$ |
| γ | 1.3×10^{-3} | $\text{W}^{-1} \text{m}^{-1}$ |
| g_b/A_{eff} | 0.10 | $\text{W}^{-1} \text{m}^{-1}$ |
| $\nu_b = \Omega_b/2\pi$ | 10.85 | GHz |
| $\Gamma_b/2\pi$ | 28.0 | MHz |
| L | 30.7 | m |
| \mathcal{F} | 177 | – |
| $\alpha = \Lambda/2 = \pi/\mathcal{F}$ | 1.8×10^{-2} | – |
| θ | 1.0×10^{-2} | – |
| P_{in} | 550 | mW |
| P_{noise} | 100 | μW |

TABLE S1: Simulation parameters.

VI. ADDITIONAL FIGURE

The additional Fig. S3 provides a further comparison between the experiments and simulations based on the mean-field model Eqs.(A1)-(A2) of the main manuscript, as well as insight into the pattern formation. Fig. S3(a) shows the powers, experimentally measured in the cavity through port (PD₂, forward signal, blue curve) and in the third port of the first circulator (PD₁, backward signal, red curve), as the detuning is scanned from left to right. This is the same scan as in Fig. 2 (b) of the main manuscript. The corresponding simulation with the parameters of Table S1 is given in Fig. S3(b). As can be seen, the agreement is very good, with the simulation reproducing faithfully the transient starting dynamics of the Brillouin laser during the detuning scan, or the soliton step and the decay of the backward Brillouin signal for positive detunings. This provides a direct validation of the mean-field model presented in this study.

From simulations, we can analyze in the spectral domain the interplay between the Brillouin cascade and the dynamics of the CSs pattern formation during a resonance scan. Fig. S3(c) shows that the S_2 threshold is crossed before the spontaneous modulation instability (MI) can take place in the resonator [and that it is simultaneously

crossed with the S_1 threshold by comparison with Fig. S3(b)]. Further increasing the detuning, the thresholds of S_4 and S_6 are crossed and four-wave mixing generates the anti-Stokes waves. As can be seen these spectral lines seed the soliton spectral comb thus setting the pattern periodicity close to twice the Brillouin frequency shift. The spectral density at $\delta = 0.45$ is display in Fig. S3(d) for the forward and the backward intra-cavity fields. We see that only the first two Brillouin thresholds (S_1 , S_2) are crossed at this detuning when CSs are circulating in the cavity. In contrast, up to four Stokes waves are generated without cavity solitons. This shows the competition between CSs and the Brillouin cascade lasing.

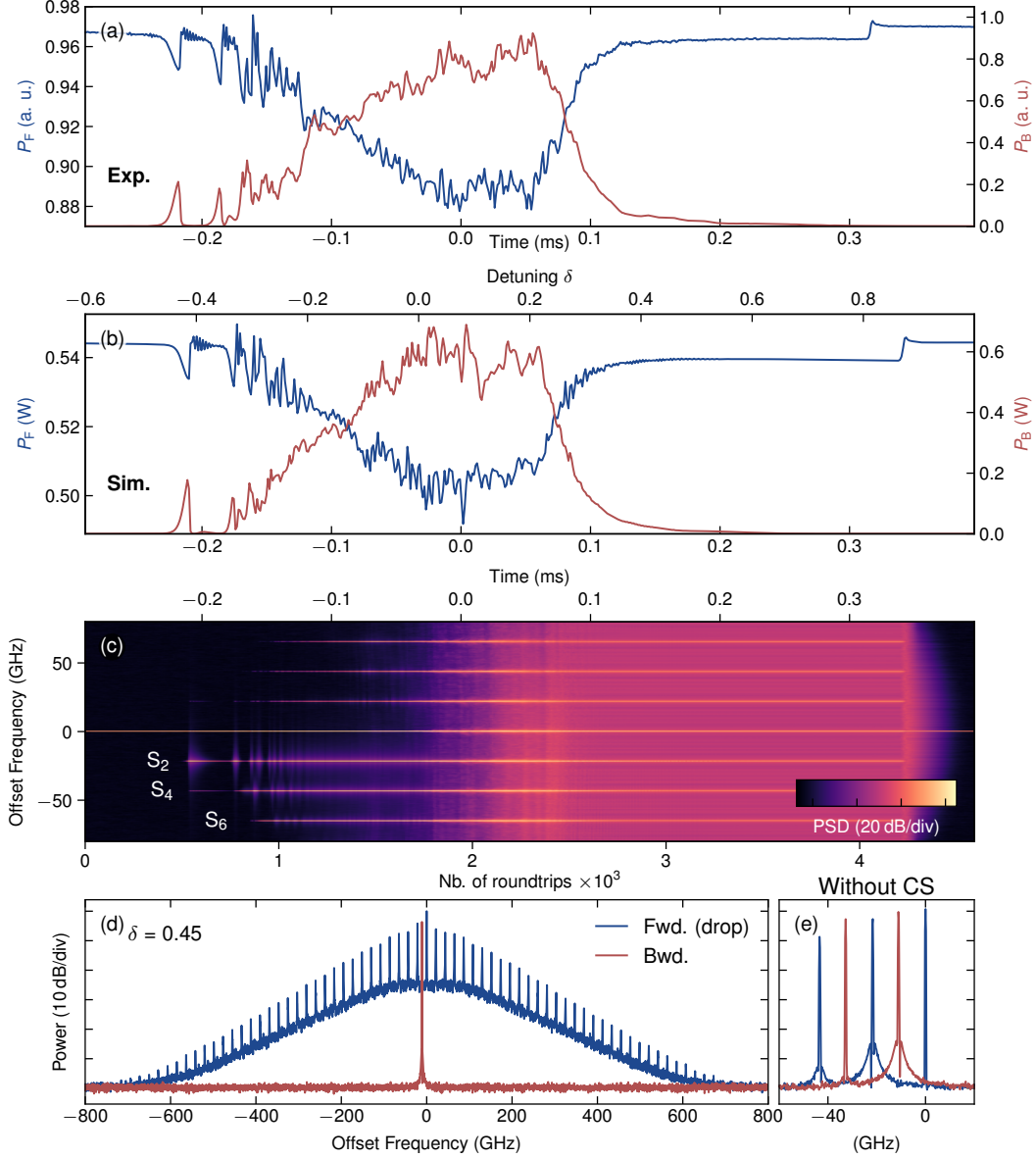


FIG. S3: (a) Experimentally recorded transmitted (P_F) and reflected (P_B) signals when scanning the frequency resonance. (b) Corresponding numerical simulation with the mean-field model. (c) Evolution of the cavity power spectral density of ψ_F during the scan shown in (b). (d) Simulated PSDs in a stabilized cavity at $\delta = 0.45$ after a detuning *scan-stop*. (e) Same as in (d) but without Kerr effect ($\gamma = 0$), thus without CSs.

- [2] J. K. Jang, M. Erkintalo, J. Schröder, B. J. Eggleton, S. G. Murdoch, and S. Coen, All-optical buffer based on temporal cavity solitons operating at 10 Gb/s, *Optics Letters*, Vol. 41, Issue 19, pp. 4526-4529 10.1364/OL.41.004526 (2016).
- [3] M. Conforti, T. Bunel, A. M. Perego, and A. Mussot, Fast and accurate modeling of Kerr-Brillouin combs in Fabry-Perot resonators, *Physical Review A* **112**, 033526 (2025).
- [4] M. Dong and H. G. Winful, Unified approach to cascaded stimulated Brillouin scattering and frequency-comb generation, *Physical Review A* **93**, 043851 (2016).
- [5] W. Firth, Stability of nonlinear fabry-perot resonators, *Optics Communications* **39**, 343 (1981).
- [6] W. J. Firth, J. B. Geddes, N. J. Karst, and G.-L. Oppo, Analytic instability thresholds in folded kerr resonators of arbitrary finesse, *Physical Review A* **103**, 023510 (2021).
- [7] L. A. Lugiato, F. Prati, and M. Brambilla, *Nonlinear Optical Systems* (Cambridge University Press, 2015).
- [8] Z. Ziani, T. Bunel, A. M. Perego, A. Mussot, and M. Conforti, Theory of modulation instability in kerr fabry-perot resonators beyond the mean-field limit, *Physical Review A* **109**, 013507 (2024).
- [9] Y. K. Chembo and C. R. Menyuk, Spatiotemporal lugiato-lefever formalism for kerr-comb generation in whispering-gallery-mode resonators, *Physical Review A* **87**, 053852 (2013).
- [10] J. Hult, A Fourth-Order Runge-Kutta in the Interaction Picture Method for Simulating Supercontinuum Generation in Optical Fibers, *Journal of Lightwave Technology* **25**, 3770 (2007).